



# Photocatalytic Performance of Hydrothermal Temperature Dependent Dip Coated TiO<sub>2</sub> Thin Films

Sayari Biswas<sup>1</sup> · Asit Kumar Kar<sup>1</sup>

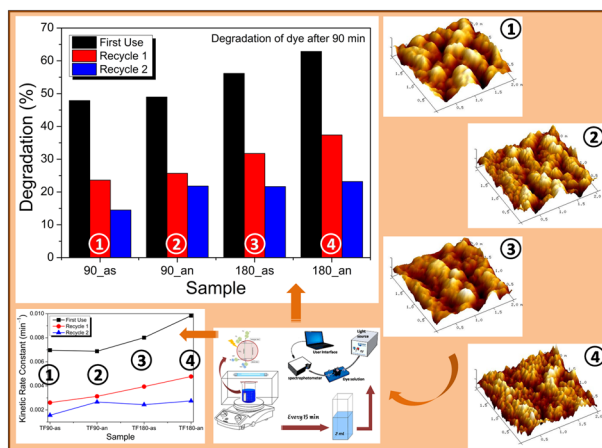
Received: 5 April 2021 / Accepted: 10 March 2022 / Published online: 12 April 2022

© The Author(s), under exclusive licence to Springer Science+Business Media, LLC, part of Springer Nature 2022

## Abstract

Anatase titania thin films were prepared by hydrothermal assisted sol-gel dip coating at two different hydrothermal temperatures: 90 °C and 180 °C for 12 h each. Some of the as-deposited films were annealed at 500 °C for 6 h. Both as-deposited and annealed films consisted of tiny spherical particles. Crystallite size and particle size increased with increased hydrothermal temperature and annealing. Atomic force microscopy showed that root mean square and average surface roughness increased with increased hydrothermal temperature and annealing. The prepared films exhibited almost zero transmittance in the violet-ultraviolet transition region with a gradual rise in the visible region up to a maximum value of ~40% at the near infrared. The transmission decreased for annealed films and as hydrothermal temperature was increased. Band gap values did not show any significant difference before and after annealing, although they decreased with increased hydrothermal temperature. Improved crystallinity and greater packing density at higher hydrothermal temperature and annealing led to a corresponding increase in the refractive index. The intensity of photoluminescence peaks was quenched when samples were annealed and as the hydrothermal temperature increased, because of annihilation of oxygen vacant states by the ambient oxygen. Improved crystallinity diminished the number of defect sites in the films, thus reducing the amount of radiative recombination of the e<sup>-</sup>/h<sup>+</sup> pair. Annealed samples and those prepared from sols processed at higher hydrothermal temperature showed better photocatalytic activity. The maximum degradation efficiency of 62.8% was demonstrated by annealed thin films prepared from sols hydrothermally processed at 180 °C after 90 minutes of UV irradiation.

## Graphical abstract



**Supplementary information** The online version contains supplementary material available at <https://doi.org/10.1007/s10971-022-05777-1>.

✉ Sayari Biswas  
sayaribiswas@gmail.com

<sup>1</sup> Micro and Nanoscience Laboratory, Department of Physics, Indian Institute of Technology (Indian School of Mines), Dhanbad 826004 Jharkhand, India

**Keywords** TiO<sub>2</sub> thin films · Hydrothermal method · Dip coating · Anatase · Photocatalysis.

## Highlights

- Anatase TiO<sub>2</sub> was obtained in an autoclave at low temperature (90 °C). The phase remained unaltered after annealing at 500 °C and also at elevated hydrothermal synthesis temperature of 180 °C.
- Agglomerated spherical particles were produced with Gaussian type size distribution.
- Higher preparation temperature and annealing quenched the photoluminescence (PL) intensity that eventually increased efficiency of photo-degradation process.
- Efficient photodegradation was achieved only after 90 minutes of UV irradiation with a very small area thin film photocatalyst (1.5 cm × 1 cm).

## 1 Introduction

TiO<sub>2</sub> nanostructured thin films are sometimes preferable over their bulk counterparts due to enhanced surface to volume ratio and improved band transition behaviour that is important for improving the performance in several applications, particularly the surface-dependent ones. In this context their morphology, crystal structure, and stoichiometry are of particular interest since they directly influence the properties and performances of TiO<sub>2</sub> and thus deposition techniques and post-deposition modifications are very crucial in ensuring the desired properties in the films. The deposition process and conditions used, including deposition temperature and pressure, substrate, etc, have been reported to be the key features for controlling the physical properties of the films obtained [1–4].

Among several chemical routes for deposition of TiO<sub>2</sub> films, a simple, inexpensive process to achieve uniform coating is the dip coating method, which involves dipping the substrate into the precursor solution and then lifting and drying to form the thin film. This method is suitable for simultaneously coating both sides of a large area substrate at ambient pressure and temperature. Tipparach et al. [5] observed that dip coated TiO<sub>2</sub> thin films calcined at temperatures lower than 200 °C showed an amorphous structure and exhibited pure anatase phase when calcined between 350 °C and 450 °C. Touam et al. [6] observed nano-structured amorphous TiO<sub>2</sub> films by sol-gel dip coating even after annealing at temperature less than 350 °C. Pedrini et al. [7] prepared anatase titania films with very low crystallinity (almost amorphous) on soda lime glass via a two-phase sol-gel dip coating deposition and used them as photocatalysts for degradation of methylene blue (MB) dye. After 3 h of UV light exposure, a maximum degradation of 50% was achieved. Thus, almost all reports to date on as-deposited TiO<sub>2</sub> have described amorphous films.

Hydrothermal synthesis is a useful method for producing sols suitable for use in dip coating processes. It is a simple

process that can produce high quality TiO<sub>2</sub> nanocrystals. Yin et al. [8] used hydrothermal synthesis to prepare TiO<sub>2</sub> nanocrystallites starting from amorphous TiO<sub>2</sub> aggregates, leading to the formation of phase-pure anatase TiO<sub>2</sub> with a narrow size distribution. Song et al. [9] synthesized anatase TiO<sub>2</sub> film with clusters of nano-sized particles at an elevated temperature.

Most studies exploring photocatalytic performance have utilized TiO<sub>2</sub> in its bulk form. However, for practical applications, nanostructured thin films are preferable due to their easy incorporation in the system and easy withdrawal. Yu et al. [10] observed the highest photo-degradation rate constant of TiO<sub>2</sub> films (annealed at 700 °C) to be 0.002 min<sup>-1</sup>. Angulo-Ibanez et al. [11] prepared porous commercial P25-based thin film photocatalytic windows for CO<sub>2</sub> conversion and obtained a maximum of 43% degradation after 2 h of reaction, corresponding to a kinetic rate of 0.0047 min<sup>-1</sup>. Shimosako and Sakama [12] coated TiO<sub>2</sub> thin films on quartz glass with methyl red (MR) and irradiated them with UV in vacuum over a very long time period (up to 140 h). Zheng et al. [13] fabricated silver-modified nano-structured TiO<sub>2</sub> thin films and depending on the Ag/TiO<sub>2</sub> molar ratios they achieved photo-degradation of 42–65%. Kamal Baba et al. [14] achieved reasonably good photocatalytic activity for anatase TiO<sub>2</sub> thin films, but after 40 hours of reaction. Sreethawong et al. [15] obtained a maximum of 68% photocatalytic degradation after 5 h of UV irradiation by varying the P25 content in mesoporous TiO<sub>2</sub> thin films.

TiO<sub>2</sub> photocatalysis is best observed in its anatase phase. However, to transform amorphous TiO<sub>2</sub> to anatase, temperatures of at least 300–400 °C are often required. In general, as-deposited TiO<sub>2</sub> films prepared at relatively low temperature are amorphous in nature. To date, superior photocatalytic activities of anatase TiO<sub>2</sub> is generally achieved in its bulk form. Only few reports are available that demonstrate high degradation rate using TiO<sub>2</sub> thin films [16], with much longer reactions times or large area coating typically being required compared to the bulk counterpart. The study presented in this communication has been focused on preparing anatase TiO<sub>2</sub> at lower temperature

with thermal stability to achieve good photocatalytic activity. The effect of annealing and hydrothermal temperature on the morphological and optical properties was observed for TiO<sub>2</sub> thin films deposited on ITO coated glass substrate by hydrothermal assisted sol-gel dip coating. Changes in the photocatalytic activity of the films with varying deposition and post deposition conditions have also been demonstrated in this article.

## 2 Experimental section

### 2.1 Chemicals

All the chemicals used in this work were of Reagent Grade. Titanyl sulphate (TiOSO<sub>4</sub>) was used as the precursor. Other key chemicals used were ammonia (NH<sub>4</sub>OH, 3mol L<sup>-1</sup>) and hydrogen peroxide (30% H<sub>2</sub>O<sub>2</sub>). TiOSO<sub>4</sub> and NH<sub>4</sub>OH were purchased from Sigma Aldrich and H<sub>2</sub>O<sub>2</sub> was supplied by Avra Chemicals. ITO coated glass substrates were purchased from Macwin India Pvt. Ltd.

### 2.2 Synthesis

TiO<sub>2</sub> thin films were deposited by dip coating using an Apex XDip-SV1 dip coater. The sol used for dip coating was synthesized via a hydrothermal method at two different temperatures: 90 °C and 180 °C. To prepare the sol, first 5 g TiOSO<sub>4</sub> was dissolved in 100 ml of DI water at ambient temperature [17]. Next, 2.5 ml ammonium hydroxide (3mol L<sup>-1</sup>) was added, which resulted in the formation of hydrous titanium oxide [TiO<sub>2</sub>.xH<sub>2</sub>O] in the form of a white precipitate. This precipitate was collected on a filter paper and washed repeatedly with distilled water to remove excess NH<sub>4</sub><sup>+</sup> and SO<sub>4</sub><sup>-</sup> ions. The washed precipitate was homogeneously dispersed in distilled water and sufficient H<sub>2</sub>O<sub>2</sub> (30%) was added under continuous magnetic stirring to completely disperse the precipitate. After peptization for 20 h, peroxy titanate acid (PTA) sol was obtained. The resulting sol was placed in a teflon lined stainless steel autoclave and kept in a hot air oven for 12 h at the desired temperature (either 90 °C or 180 °C). These final sols were used to deposit thin films by dip-coating on ITO-coated glass substrates. This particular substrate was chosen primarily to improve the adhesion of the TiO<sub>2</sub> films. It may also find several applications in device fabrication. Dipping and lifting speeds were kept constant at 20 mm/min. Before film deposition, all the substrates were cleaned in an ultrasonic bath with acetone and isopropyl alcohol sequentially. Samples were deposited using 12 coating cycles. After deposition, the films were first dried at 60 °C for 30 min in a hot air oven. They were then annealed at 500 °C in a furnace for 6 h. Samples were also kept as-deposited for further

**Table 1** Nanostructured thin films under investigation and their processing conditions

| Sample name | Hydrothermal temperature | Annealing temperature | Annealing time |
|-------------|--------------------------|-----------------------|----------------|
| TF90-as     | 90 °C                    | NA                    | NA             |
| TF90-an     | 90 °C                    | 500 °C                | 6 h            |
| TF180-as    | 180 °C                   | NA                    | NA             |
| TF180-an    | 180 °C                   | 500 °C                | 6 h            |

studies. The details of the prepared samples are shown in Table 1.

### 2.3 Characterization

Grazing incidence X-ray diffraction (GIXRD) was used to study the crystallinity and phase identification of the samples in  $\theta$ -2 $\theta$  scanning mode using Bragg-Brentano configuration, with the incidence angle kept fixed at 2°. The scan was run between 10° and 80° 2 $\theta$  at 0.02° intervals with a PANalytical X'Pert diffractometer with CuK <sub>$\alpha$ 1</sub> ( $\lambda$  = 0.154056 nm) radiation.

The surface morphology of the films was studied by FE-SEM Supra 55 and Dimension ICON Atomic Force Microscopy (Bruker). For better understanding of the surface topography, a variety of scans were carried out at random locations on the film surface, keeping the scanned area constant at 2  $\mu$ m  $\times$  2  $\mu$ m. The obtained data were converted into NanoScope Analysis software (Version 1.4) to analyze different parameters such as the root mean square roughness (R<sub>q</sub>), average roughness (R<sub>a</sub>), surface skewness (R<sub>sk</sub>) and kurtosis (R<sub>ku</sub>).

The absorbance and transmission spectra of the deposited films were collected using an Agilent Cary 5000 UV-Vis spectrophotometer. To determine the defect levels in the synthesized TiO<sub>2</sub> films, photoluminescence emission spectra was recorded in the wavelength range 300–600 nm with an excitation wavelength of 260 nm on a Horiba-2500 Acton fluorescence spectrometer with a 150 W Xe lamp. Refractive indices and the extinction coefficients were also calculated from the recorded absorbance spectra.

The photocatalytic activities of the prepared thin films were analyzed by decomposition of aqueous solution of methylene blue (MB) dye. Initially, 100 ml of an aqueous 1.5  $\times$  10<sup>-6</sup> M methylene blue was prepared and stirred for 15 minutes. The TiO<sub>2</sub> thin films were placed in the solution with the help of a copper holder and exposed under UV light. 5 ml of the solution was taken from the total solution at the regular interval of 15 min until a total duration of 90 min. UV-Vis absorption spectra of the collected solutions were recorded in the range 500–800 nm to evaluate the degradation rate of the dye with an Ocean Optics HR4000 UV-Vis spectrophotometer and DH-2000-BAL light

source with deuterium (25 W) and tungsten halogen lamps (20 W) combined in a single light source, which is able to be operated with stable output within the wavelength range 215–2000 nm.

### 3 Results and discussion

#### 3.1 Crystal structure

Figure 1 depicts the GIXRD profiles of the TiO<sub>2</sub> thin films. For ease of representation, individual profiles (b)–(d) have been shifted along the Y-axis. The GIXRD peaks showed that the anatase phase is formed without any contamination by other phase of TiO<sub>2</sub> in all samples (JCPDS 84-1285). No other forms of titanium oxides, such as Ti<sub>3</sub>O<sub>5</sub>, Ti<sub>2</sub>O<sub>3</sub> and TiO, were detected and no amorphous background was evident. Most previous studies found the as-deposited films to be amorphous and even in some cases, lower temperature annealing (200–300 °C) did not enhance the crystallinity [18, 19]. In contrast, in our study we found the films to be anatase even in the as-deposited conditions, which has been only rarely reported previously [20].

To obtain more detailed information about the structure of the coatings, the crystallite sizes were estimated from the FWHM of the XRD peaks (101), (004), (200), (105), (211), (204), (116), (220) and (215) using the Scherrer formula:

$$D = \frac{K\lambda}{\beta_{hkl}\cos\theta}$$

Here  $\beta_{hkl}$  is the peak width at half of maximum intensity (FWHM),  $K = 0.94$ ,  $\lambda$  is the wavelength of the incident X-ray (0.1542 nm) and  $D$  is the crystallite size. Thermal treatment of the sol increases the crystallite size. For samples prepared from the 90 °C sol, the crystallite size was found to be 14 nm and 17 nm for as-deposited and annealed films, respectively. For samples made from the 180 °C sol, the values are 17 nm and 18 nm, respectively (Table 2). For the second case, the higher hydrothermal temperature introduces larger nanocrystals. Similarly, annealing also has an effect on crystallization of the films. Crystallite size increases as a result of relaxation of grain boundaries due to increased thermal energy.

#### 3.2 Morphological study

Figure 2 shows FESEM top view images of the films, prepared from both the sols (90 °C and 180 °C). Irrespective of hydrothermal temperature all the samples were found to consist of spherical or near-spherical particles. During hydrothermal processing, the spontaneous nucleation led to aggregation of crystallites and in our case they agglomerated in spherical or almost spherical shape.

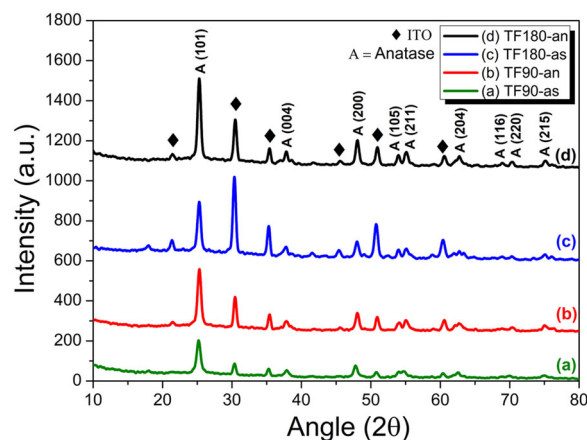


**Fig. 1** GIXRD profiles of the samples made from 90 °C and 180 °C sol – (a) 90-as and (b) 90-an (c) 180-as and (d) 180-an

Spherical nanostructures were distributed in a closely packed manner on the film surface for all the samples. For the films made from the 180 °C sol, larger particles were observed. But comparing as-deposited films made from both sols, it was observed that the agglomerate size increased when the hydrothermal temperature used for sol preparation increased or when the samples were annealed. This variation in agglomerate size of the TiO<sub>2</sub> nanoparticles, as shown in Fig. 4, can be explained on the basis of a change in reaction rate or increased super-saturation of reactants due to which a large number of ions are available for nucleation and which may cause the increment in particle size. Indeed, the driving force for nucleation and growth phenomena is super-saturation. For a supersaturated solution maintaining a particular temperature, particles stop growing when they achieve a minimum free energy condition and maintain equilibrium with the surroundings. Therefore, a change in temperature is required as the driving force of crystallization to recommence the growth process. Thus, with increased hydrothermal and/or annealing temperature, crystallites and their agglomerates tended to increase in size via dissolution/re-precipitation processes.

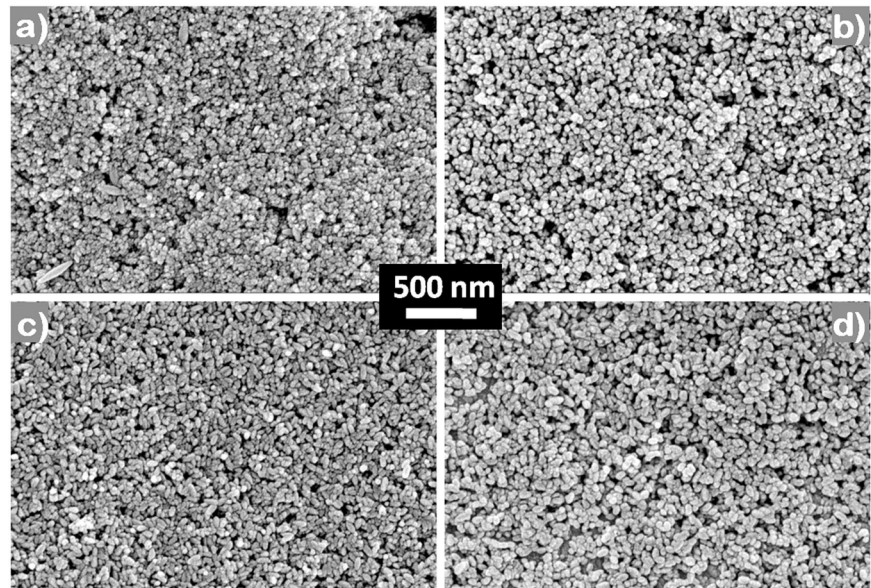
With increasing hydrothermal temperature, the presence of some small voids was observed in all the samples. These voids appeared due to the increment in particle size and layered structure of the films. Our films were made by depositing several layers of the sol containing TiO<sub>2</sub> particles. When particle sizes were small at lower hydrothermal temperature, they readily fitted into the interstitial voids of the previous layer. But for larger particles, the interstitial sites were too small to accommodate them and the voids remained open. Consequently, in the samples made from the 180 °C sol, voids were more prominent in the corresponding FESEM images. These voids provided additional effective surface area.

Particle size histograms were constructed (Fig. 3) by calculating the particle sizes from FESEM images for all



**Table 2** Values of RMS roughness, Average roughness, average crystallite size, and band gap of the prepared thin film samples

| Sample Name      | $R_q$ in nm | $R_a$ in nm | $R_q/R_a$ | Avg. Crystallite Size (nm) | Band Gap (eV) |
|------------------|-------------|-------------|-----------|----------------------------|---------------|
| 90 deg-as dep    | 22          | 18          | 1.26      | 14                         | 3.24          |
| 90 deg-annealed  | 47          | 37          | 1.26      | 17                         | 3.22          |
| 180 deg-as dep   | 34          | 27          | 1.27      | 17                         | 3.13          |
| 180 deg-annealed | 76          | 60          | 1.27      | 18                         | 3.08          |

**Fig. 2** FESEM top view of samples (a) TF90-as, (b) TF90-an, (c) TF180-as and (d) TF180-an

samples using ImageJ software. For each sample, the diameters of 250 particles were measured using FESEM images of different magnifications with the help of the said software to generate the particle size histograms. The narrow and nearly symmetric histogram for the as-prepared samples made from the 90 °C sol (TF90-as) indicated that the sizes of the particles (more precisely, particle agglomerates) on the film surface were relatively homogeneous in comparison to the other films. Annealing (sample TF90-an) increased the width of the histogram, indicating more scattering in the particle size distribution. The histograms also shifted towards higher values, revealing that the average agglomerate size increased from 26 nm to 37 nm for samples TF90-as and TF90-an. For samples made from the 180 °C sol, this increment was from 57 nm to 72 nm for samples TF180-as and TF180-an, respectively. Hence, as hydrothermal temperature increased from 90 °C to 180 °C, the increment in agglomeration size was almost 30 nm. For these samples, the width of the histograms were more than the samples made from the 90 °C sol. Average agglomeration size and average crystallite size (from XRD) are presented in Fig. 4.

Figure 5 shows the EDAX spectra for TiO<sub>2</sub>/ITO samples. Besides Ti and O, these showed evidence of the presence of C, Si, Au and In. Since we used indium tin oxide coated

glass substrates, the presence of In and Si is expected. Au was observed due to the gold used to coat the samples prior to imaging. No additional elements were evident.

### 3.3 AFM study

The surface morphology and topography of the deposited films were studied by atomic force microscopy using contact mode. Two-dimensional (2D) and three-dimensional (3D) AFM images are shown in Fig. 6. The 3D images show that the surface of the TiO<sub>2</sub> films exhibits hills and valleys. The corresponding 2D images (not shown here) reveal that the films have nanocrystalline granular morphology and TiO<sub>2</sub> particles are uniformly distributed all over the surface. The films were mainly composed of spherical particles. The surface roughness of the films increased when the annealing temperature increases.

The roughness of the prepared samples varies with hydrothermal temperature. Post-deposition thermal annealing also affects the film roughness. For samples prepared from 90 °C sol with 12 coatings, RMS roughness was observed to be ~47 nm and ~22 nm for annealed and as-deposited samples, respectively. For the corresponding samples,  $R_q$  increases to ~76 nm and ~34 nm, respectively, when the hydrothermal temperature is increased to 180 °C.

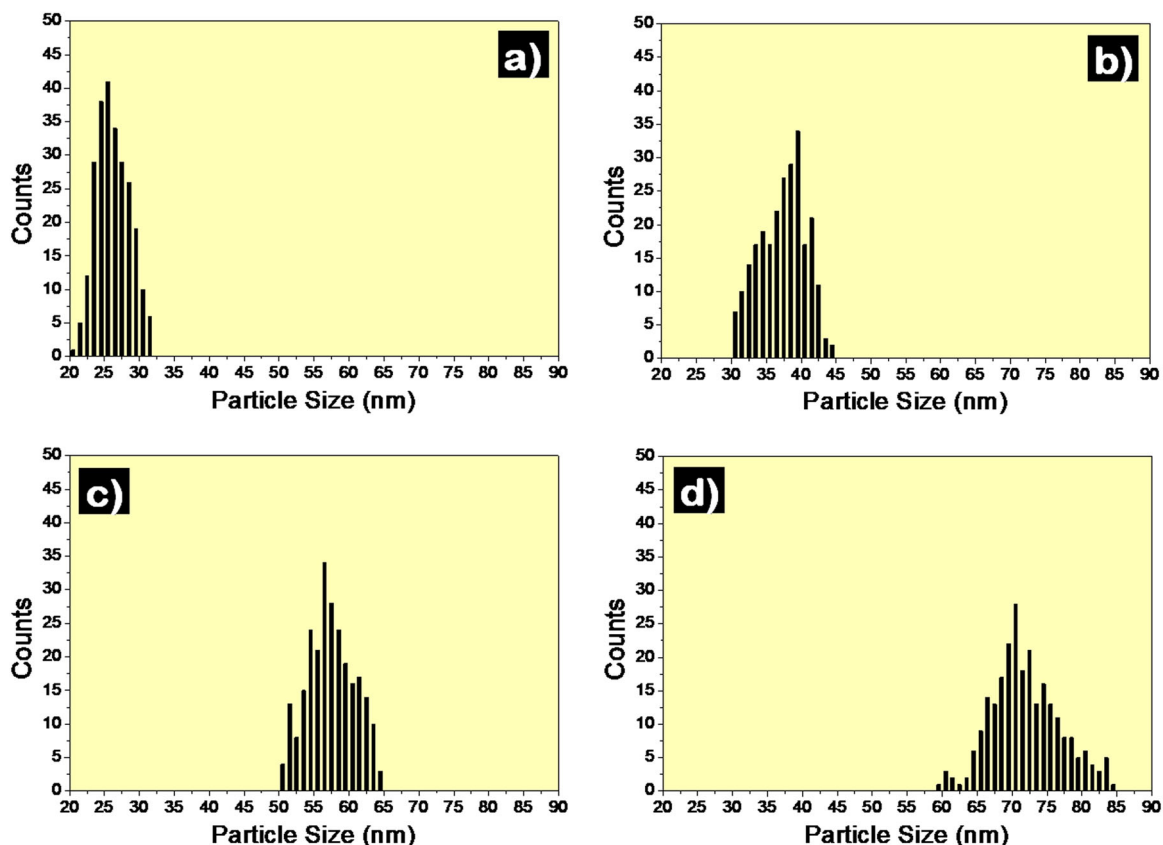


Fig. 3 Particle size distribution histogram obtained from FESEM top view of samples (a) TF90-as, (b) TF90-an, (c) TF180-as and (d) TF180-an

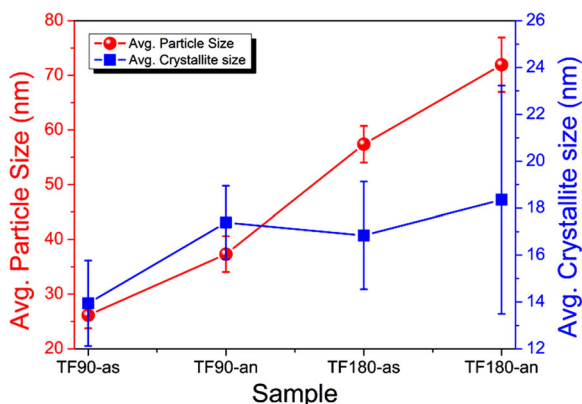


Fig. 4 Graphical representation of average agglomeration size obtained from FESEM and average crystallite size (from XRD) of the samples

The values of average roughness,  $R_a$  for these samples are ~37 nm, ~17 nm, ~60 nm and ~27 nm, respectively. Sample roughness (both  $R_a$  and  $R_q$ ) increases after annealing. This increment might be a result of increased particle size and improved crystalline nature of the films, as shown by previous studies [21, 22]. Lin *et al.* [23] reported that the high temperature can enhance the migration of grain boundaries resulting in the coalescence of grains.

If the roughness profile follows a Gaussian distribution,  $R_a$  and  $R_q$  are related via:

$$R_q \approx \sqrt{\frac{\pi}{2}} R_a \approx 1.25 \times R_a$$

i.e., according to the statistical theory, the ratio of  $R_q$  to  $R_a$  should be 1.25, for a Gaussian distribution of surface particles [24, 25]. Ward [26] noticed that most engineered surfaces possess approximately a Gaussian height distribution with  $R_q/R_a$  values of up to 1.31. As shown in Table 2, the values of  $R_q/R_a$  for the present samples are reasonably close to 1.25. This result indicates a Gaussian height distribution of the film surfaces, at the imaging scale. To verify this, we obtained surface height histogram from the AFM images and fitted a Gaussian curve to the envelope of the histogram which matched very closely (Fig. 7).

Skewness is a dimensionless quantity, which in general is evaluated as positive or negative values and evaluates the symmetry of a surface distribution. For negative skewness, the valleys are dominant over the scanned area, and the peaks are dominant when it is positive [27]. Our samples are valley dominant as all of them possess negative skewness values.

Kurtosis is a measure of the sharpness of the roughness profile of the surface. When the value of Kurtosis ( $R_{ku}$ ) for a

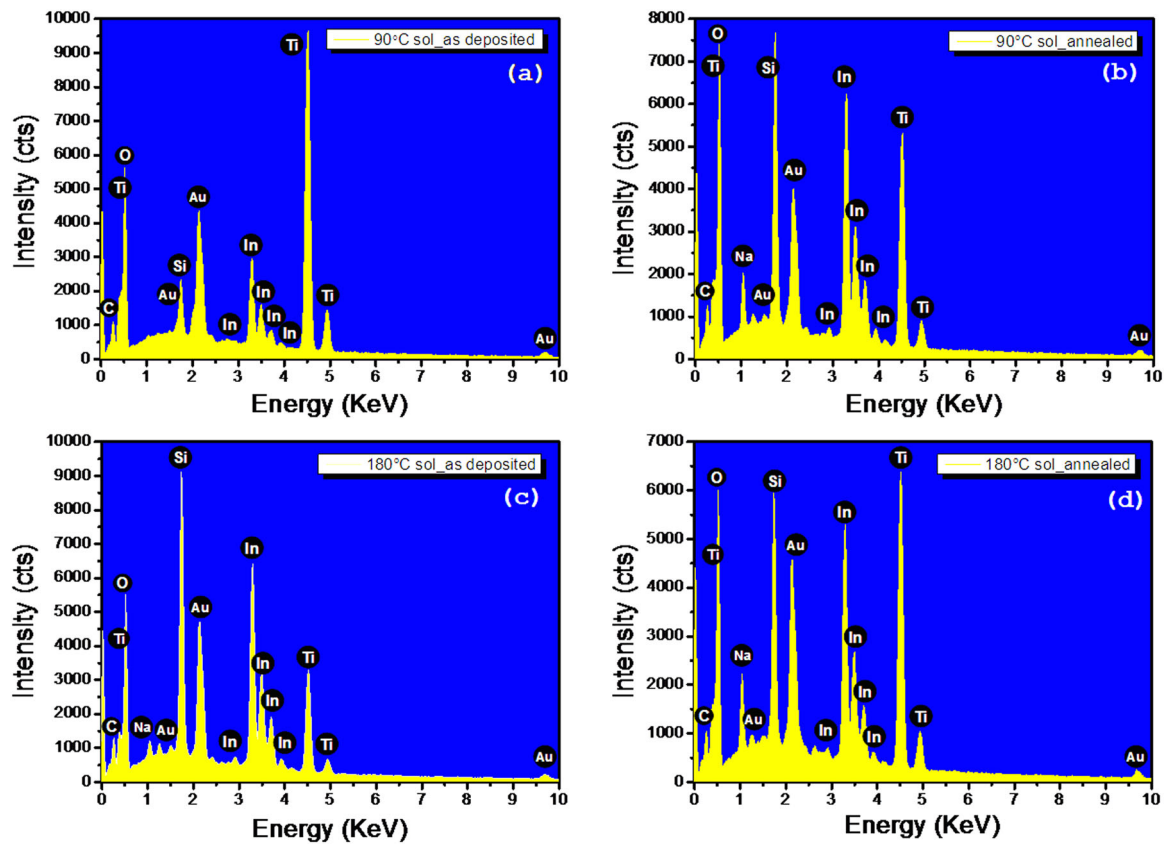


Fig. 5 EDAX spectra of the samples (a) TF90-as, (b) TF90-an, (c) TF180-as and (d) TF180-an

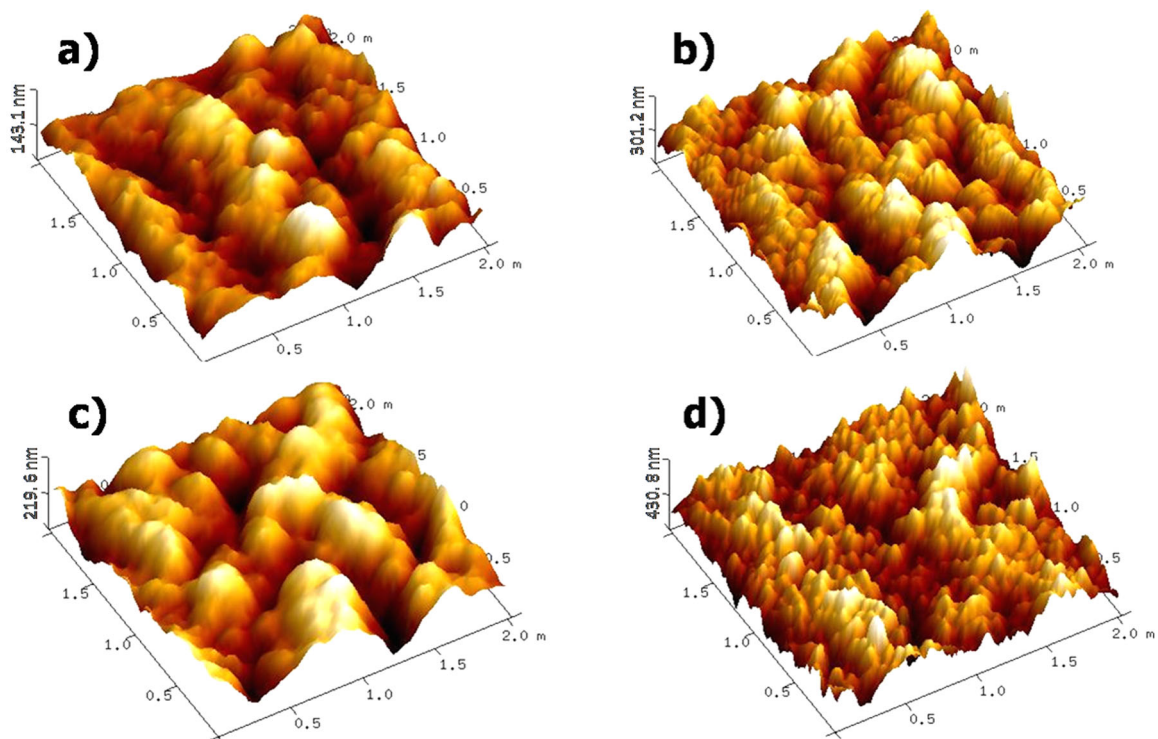
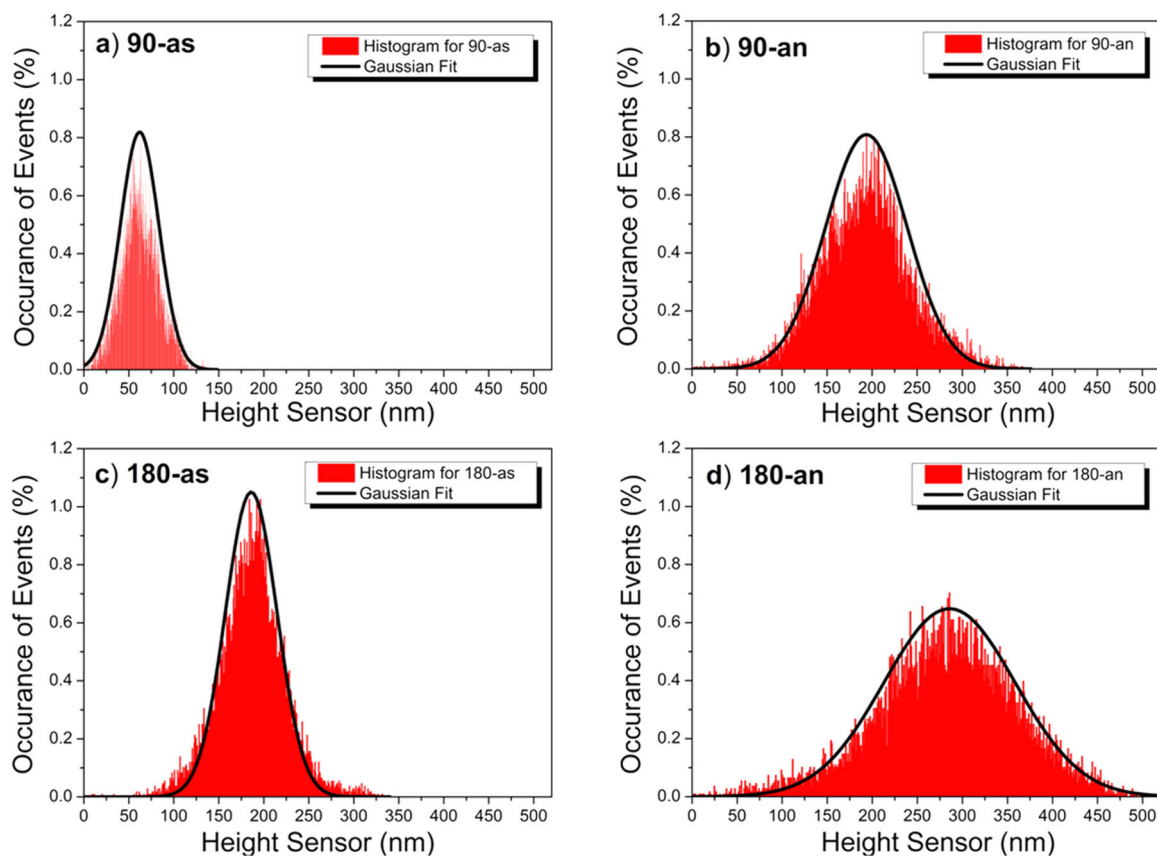


Fig. 6 AFM 3D images showing the surface profiles of (a) TF90-as, (b) TF90-an, (c) TF180-as and (d) TF180-an



**Fig. 7** Height histogram from AFM images and their corresponding Gaussian Fit for the samples (a) 90-as (b) 90-an (c) 180-as and (d) 180-an

surface is below three, it indicates that the scanned area has relatively fewer high peaks and low valleys, indicative of a bumpy surface. When  $R_{ku}$  is greater than three, the surface will have higher numbers of high peaks and deep valleys, characterizing a spiky surface. All of our samples appear to follow the second case. These values of RMS roughness and average roughness along with the crystallite size obtained from XRD studies have been graphically represented in Fig. 8.

### 3.4 Optical properties

Figure 9 shows the transmission spectra of the deposited samples. The spectra of the thin films show a gradual rise starting at the violet-ultraviolet region from almost no transmission to a maximum of ~40% at the near-infrared. This maximum transmittance value was observed for as-deposited sample made from the 90 °C sol and it decreases with increased hydrothermal temperature and annealing. The FESEM images reveal that particle size increases with annealing and this eventually increase the amount of scattered light. Film uniformity decreased with increased hydrothermal temperature and also after annealing, thus enhancing the amount of scattered light. The loss of light

due to scattering and absorbance results in a decrease in the transmittance. In summary, enhancement of both absorbance and scattering loss is the result of increased surface roughness as indicated by AFM studies. The transmittance edge slightly shifts towards longer wavelength as a consequence of annealing and higher hydrothermal temperature. Previous studies suggested that both scattering and absorption loss increase as a result of increasing surface roughness [28]. Additionally, at higher hydrothermal temperature, the presence of a large number of oxygen vacancies absorbs the incident light [29, 30] which leads to a decrease in transmittance.

The optical band gaps ( $E_g$ ) of the films was calculated using the Tauc relation:

$$(\alpha h\nu)^{1/2} = \text{const.} \times (h\nu - E_g)$$

where  $\alpha$  is the absorption coefficient. For the as-deposited film made from the 90 °C sol, the value was found to be 3.24 eV. For the same film annealed at 500 °C, the value was essentially identical (3.22 eV). For the films made from the 180 °C sol, the corresponding values are 3.13 eV and 3.08 eV, respectively (Fig. 10). The band gap decreased when the hydrothermal temperature was increased, but for



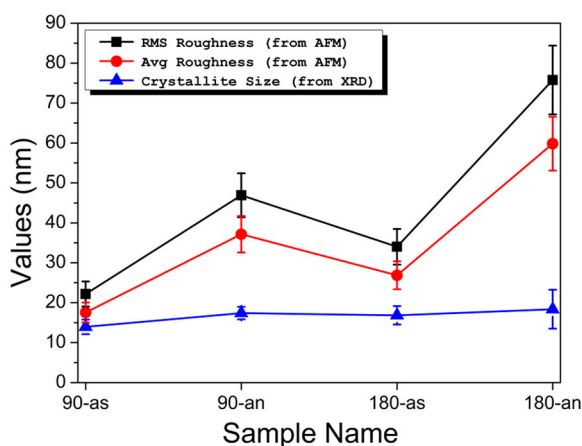


**Fig. 8** Graphical representation of RMS roughness, average roughness and crystallite size of the thin films TF90-as, TF90-an, TF180-as and TF180-an obtained from AFM and XRD

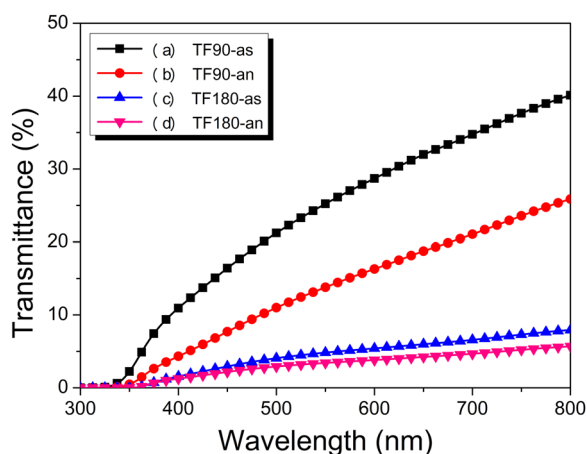


**Fig. 9** Wavelength dependent transmittance spectra of (a) TF90-as, (b) TF90-an, (c) TF180-as and (d) TF180-an

the film made from the same sol there is no significant change in the band gap value. This is due to larger particle size and thermal stress in the films deposited from sols processed at higher hydrothermal temperature. The increase in particle size is clearly observed in the FESEM images. In a single atom, the optical band gap is equal to the energy difference between the ground state and the first excited state. But in bulk systems, both levels are broadened, forming a band. As particle size increases, broadening of the bands also becomes greater, decreasing the separation between the conduction band minima and valence band maxima, leading to a decrease in the band gap energy.

The average crystallite size increased with annealing temperature, as was clear from the XRD study. When nanoparticles and thin films develop during their processing, the coalescence of grains and dislocations at the boundaries of two grains take place. Dislocations may also happen in the crystal lattice at the film–substrate interface to relieve the strain. The

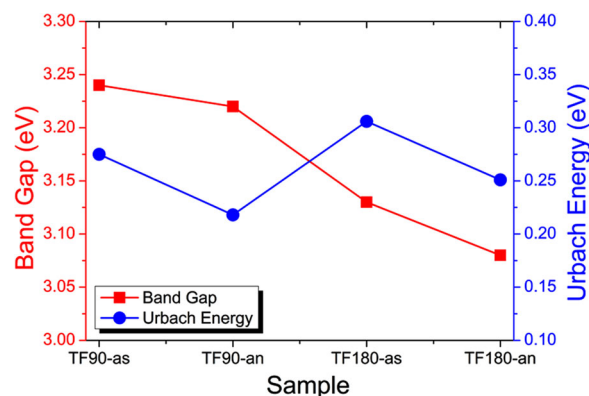


**Fig. 10** Graphical representation of variation of Band Gap and Urbach Energy values of the samples TF90-as, TF90-an, TF180-as and TF180-an

number of dislocation lines intersecting a unit area in the crystal is the dislocation density ( $\delta$ ) in the film which is closely related to the crystallite size ( $D$ ),  $\delta = n/D^2$ , where  $n$  is a constant and for minimum dislocation density  $n = 1$ .

Earlier studies inferred that for high dislocation density, dilation occurs in the atomic spacing, which is an influencing factor for the band gap nature of the materials. If the dislocation density is high for a certain material, it should possess higher band gap [31]. The decrease in optical band gap on annealing and for higher hydrothermal temperature is consistent with a decrease in dislocation density.

The Urbach Energy values ( $E_u$ ), which may be used to quantify the degree of disorder in the band edge of semiconductors, were determined for all samples using Urbach's empirical rule,

$$\ln\alpha = \ln\alpha_0 + \frac{h\nu}{E_u}$$

The slope of the linear portion of  $\ln\alpha$  vs.  $h\nu$  gives us the Urbach energy values. The calculated values were 275 meV, 218 meV, 306 meV and 251 meV for samples 90-as, 90-an, 180-as and 180-an, respectively (Fig. 10). Urbach energy values are slightly larger in the case of samples made from the higher temperature sol. With increasing hydrothermal processing temperature, Urbach energy values increased, keeping parity with the decrease in band gap. This indicates that more disordered states are accumulated near the band edges causing the observed narrowing of band gap values. But annealing decreased the Urbach energy values without much alteration in the band gap values. This is an anomalous situation. Kabir et al. [32] also noted this trend for Al-doped ZnO thin films. This decrement happened due to annealing-induced increase in crystallinity which was also evident from the XRD studies. Annealing decreases the Urbach Energy values, consistent with better crystallinity. This fact has also been supported by XRD studies [33, 34].

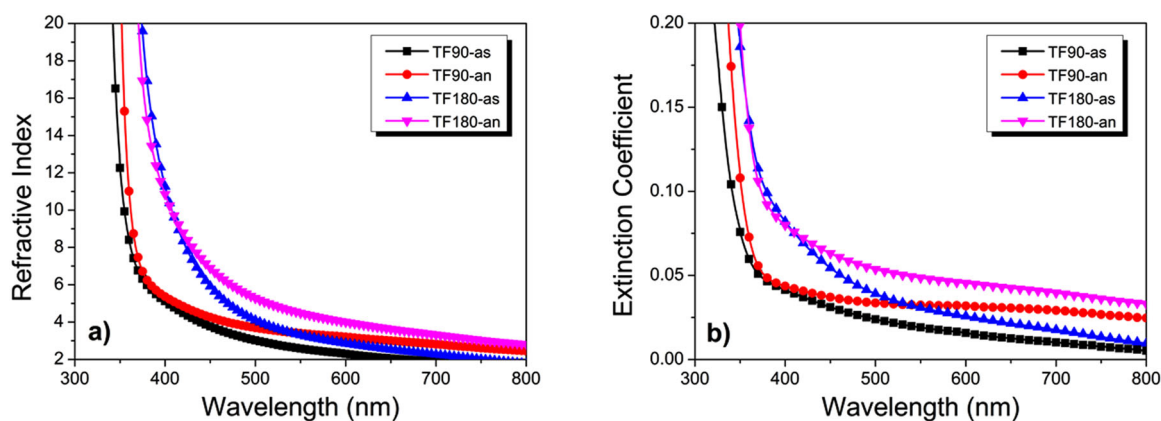


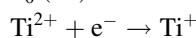
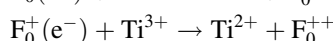
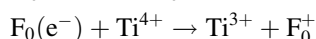
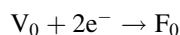
**Fig. 11** Spectral dependence of (a) refractive index and (b) extinction coefficient of samples TF90-as, TF90-an, TF180-as and TF180-an

Both the refractive indices and extinction coefficients of the films decreased with increasing wavelength. The spectral dependence these parameters are shown in Fig. 11. In the lower wavelength region (i.e. higher incident energy) due to resonance phenomenon between the incident electromagnetic radiation and the electron polarization in the material, coupling of electrons takes place. This leads to attenuation in the propagation of the electromagnetic wave through the material. Thus, both refractive index and extinction coefficient showed higher values at lower wavelengths. Refractive index values were observed to increase with an increase in hydrothermal temperature and also with annealing. This is due to improved packing density and crystallinity of the films as a result of annealing. As indicated above, annealing in atmospheric condition also decreased the number of oxygen vacancies, which would also be expected to result in an increase in the refractive index [35]. In addition, the refractive index increase with annealing temperature is consistent with the Moss rule which states  $E_g n^4 \sim \text{constant}$  [36]. Extinction coefficient also exhibited a similar trend to that of the refractive index. Increasing film roughness due to thermal treatment results in more light scattered from the surface. Thus, the extinction coefficient also increases with annealing. The thin films showed relatively high refractive indices, which suggests a potential application as an intermediate layer to enhance the light extraction efficiency (LEE) of a typical bottom-emitting organic light emitting diode (OLED).

Figure 12 shows the PL spectra for all the films in the wavelength range 350 – 600 nm, while the deconvoluted spectra, fitted with appropriate Gaussian functions, are illustrated in Fig. 13. Photoluminescence is mostly a surface phenomenon where a change in surface states plays a key role in the luminescence. As our samples were prepared under hydrothermal condition, oxygen vacancies and surface hydroxyl groups are dominant sites for trapping excitons [37]. For all the samples, a band edge transition was observed at

380 nm (3.26 eV, peak 1). Other peaks appeared due to several types of defect levels mostly related to self-trapped excitons (STE), surface states and oxygen vacancies [38]. Just below the excitonic emission, another peak at 398 nm (3.1 eV, peak 2) was observed resulting from the interband electrons trapped at the deep acceptor level. The 415 nm (2.99 eV, peak 3) and 422 nm (2.95 eV, peak 4) peaks are due to self-trapped excitons that resulted from the charge-transfer transition from  $\text{Ti}^{3+}$  to oxygen anions in a  $\text{TiO}_6^{8-}$  complex [39, 40]. Zuo et al. [41] also reported the presence of such a band associated with  $\text{Ti}^{3+}$  sites just below the conduction band minima. Theoretical studies by Justicia and team also supported the presence of these types of bands [42].

Transitions at 440 nm (2.8 eV, peak 5) are due to STEs which occur when a  $\text{Ti}^{3+}$ -3d electron de-excites to the valence band. The emission bands at 452 nm (2.75 eV, peak 6), 463 nm (2.7 eV, peak 7), and 470 nm (2.64 eV, peak 8) are also due to STEs. For all samples, they are associated with transitions involving surface states and occurred due to the recombination of trapped electrons arising from unsaturated bonds on the surface of the  $\text{TiO}_2$  nanoparticles. When exposed titanium sites ( $\text{Ti}^{4+}$ ) on the surface of the thin film are changed into lower valency sites ( $\text{Ti}^{3+}$ ,  $\text{Ti}^{2+}$ , and  $\text{Ti}^+$ ), localized energy levels are introduced within the forbidden gap. Oxygen vacancies in the  $\text{TiO}_2$  lattice generate F-centres ( $\text{F}_0$ ) by capturing an electron pair. One of the electrons from the electron pair trapped in the oxygen vacancies can migrate to the adjacent  $\text{Ti}^{4+}$  yielding  $\text{Ti}^{3+}$  and  $\text{F}_0^+$  centres (oxygen vacancies associated with a single electron). On further capture of an additional electron  $\text{Ti}^{3+}$  turns into  $\text{Ti}^{2+}$  with the creation of  $\text{F}_0^{++}$  centres.



These trap states are influential contributors in the luminescence of TiO<sub>2</sub> which give rise to the mentioned bands in the observed spectra.

Peaks at 485 nm (2.55 eV, peak 9) and 495 nm (2.5 eV, peak 10) mainly result from the self-trapped excitons and oxygen vacancies. Due to the self-trapping, excitons lose

energy via lattice relaxation processes and as a result, the PL peak is observed at higher wavelengths. The 534 nm (2.35 eV, peak 11) and 544 nm (2.28 eV, peak 12) peaks are the results of de-excitation from lower vibronic states in oxygen vacancies to the ground state of the TiO<sub>2</sub> lattice. The emission mechanism has been depicted in the band diagram in Fig. 14.

For a better comparison of the relative emission intensities with respect to the excitonic emissions, the ratios  $I_{UV}/I_{violet}$ ,  $I_{UV}/I_{blue}$  and  $I_{UV}/I_{green}$  were calculated from the deconvoluted spectra (Fig. 13) for all of the samples. The calculated intensity ratio values are given in Table 3. The UV emissions in TiO<sub>2</sub> results from band edge and near band edge emissions. Thus, these relative peak intensities signify emissions from inter-band defect sites relative to the UV emissions. For TiO<sub>2</sub>, the blue emission and a part of the violet emission signifies surface state emissions and emissions due to self-defects (STEs) as described in the previous paragraph. With annealing, the  $I_{UV}/I_{vio}$  and  $I_{UV}/I_{blue}$  values decreased indicating reduced radiative recombination via the trap states related to violet and blue emissions i.e. via surface trap and STEs. We can further conclude that annealing annihilates some of these trap states because of

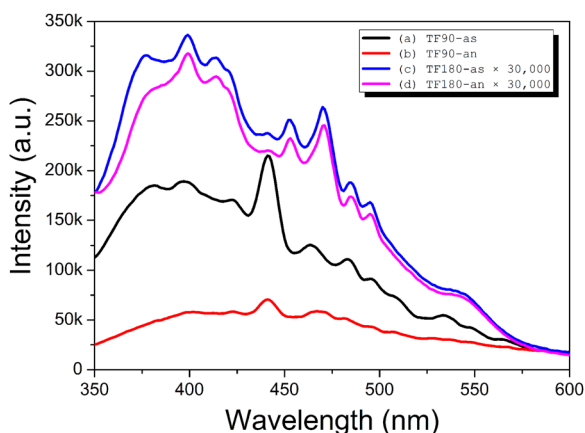


**Fig. 12** Photoluminescence emission spectra of (a) TF90-as, (b) TF90-an, (c) TF180-as and (d) TF180-an

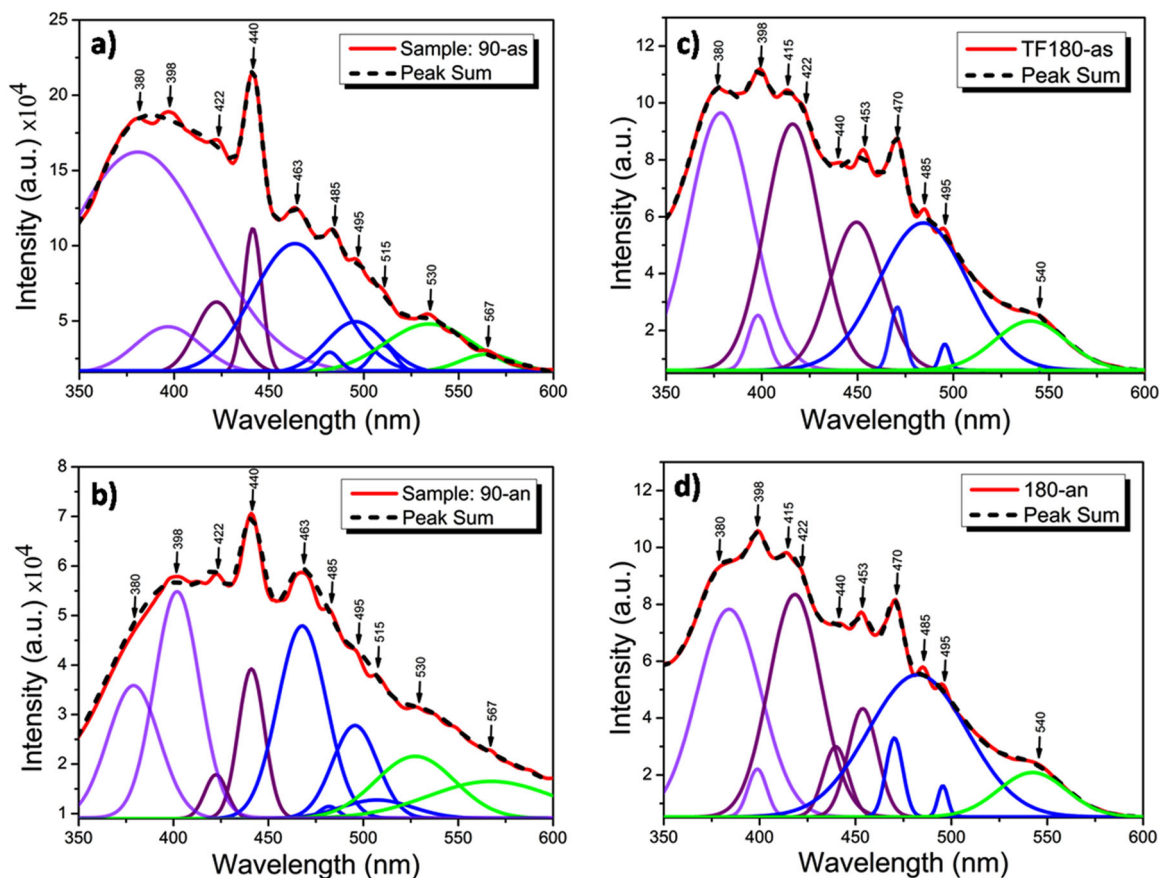


**Fig. 13** Deconvoluted photoluminescence emission spectra of (a) TF90-as, (b) TF90-an, (c) TF180-as and (d) TF180-an

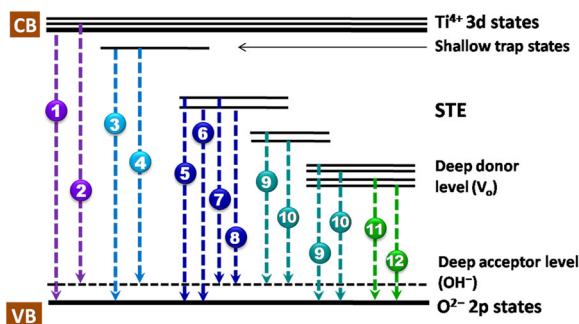


**Fig. 14** Schematic representation of the band region of the prepared thin films indicating the probable interband states contributing to the PL emission

**Table 3** Relative Intensity Ratio Values of UV Emission to different defect emissions

| Sample   | $I_{uv}/I_{vio}$ | $I_{uv}/I_{blue}$ | $I_{uv}/I_{green}$ |
|----------|------------------|-------------------|--------------------|
| TF90-as  | 2.08             | 7.40              | 8.00               |
| TF90-an  | 2.89             | 7.64              | 7.90               |
| TF180-as | 1.03             | 1.10              | 5.58               |
| TF180-an | 0.84             | 1.24              | 3.90               |

the improvement in crystal structures. Green emissions are mostly related to oxygen vacancies. Annealing and higher hydrothermal processing temperature also diminished the relative intensities of such emissions as ambient oxygen captured by the vacancies reduced the number of vacant sites and also the number of radiatively recombined excitons through these sites. The reduction in green emission intensity is more pronounced than that of violet and blue emissions.

PL intensity was found to decrease with annealing and increase with hydrothermal temperature. The quenching of luminescence intensity can be attributed to elimination of lattice defects due to annealing. The variation of PL intensity may be due to the change in shallow level defect states on the TiO<sub>2</sub> surface [43, 44]. With annealing and increased hydrothermal temperature, the significant decrease in PL intensity indicates the decrease in recombination rates due to better crystallization.

From XRD data, we observed that crystallite size (and the particle size as well) increases with an increase in hydrothermal processing temperature and also annealing temperature. In general, the density of the surface states decreases with the increase in grain size and luminescence intensity decreases with decrease of the density of the surface states. FESEM images of our samples reveal that TiO<sub>2</sub> particle size increases with increasing hydrothermal temperature. With bigger particles, the possibility of the presence of more dangling bonds increases. These bonds act as centres for non-radiative recombination and quench the PL intensities. At higher hydrothermal temperature and after

annealing, crystallinity improves, as supported by XRD data, which is consistent with a reduction in defects in the samples. This reduction further decreases the intensity of the PL peaks. Since our samples were annealed in air, during the annealing process, some of the oxygen vacancy sites are annihilated by capturing ambient oxygen, thus resulting in quenching of the PL intensities.

### 3.5 Photocatalytic activity

The photodegradation of methylene blue dye by TiO<sub>2</sub> photocatalysts is a pseudo-first-order reaction where the photodegradation rate constant ( $k$ ) can be determined by the following equation:

$$\ln \frac{C_t}{C_0} = -kt$$

where  $C_0$  and  $C_t$  are the initial concentration and the concentration at time  $t$  of the dye solution, respectively, and  $k$  is the first-order rate constant. A plot of  $\ln C_t/C_0$  vs time represented in Fig. 15 yields a linear nature, the slope of which upon linear regression determines the first-order rate constant  $k$ . Higher values of  $k$  indicate more rapid degradation.

The degradation rate of the dye is generally expressed as,

$$\text{Degradation Rate} = \frac{C_0 - C_t}{C_0}$$

The photocatalytic activities of the prepared samples were observed to increase as the hydrothermal temperature increases and also as a result of annealing. For the as-deposited and annealed samples made from the 180 °C sol, the degradation of dye was found to be 56.1% and 62.8%, respectively, after 90 mins. The corresponding values for samples made from the other sol are 47.9% and 49%, respectively. Degradation of the dye after 90 min and the kinetic rate for each sample illustrated in Fig. 15 are given in Table S1 available in the Supplementary Information.

Enhancement in photocatalytic activity depends on effective separation of photo-induced  $e^-h^+$  pairs in the dye material. PL intensities are indicative of the amount of radiative recombination. For the present case, PL intensity decreases with annealing and increases in hydrothermal temperature, suggesting a decrease in recombination of the  $e^-h^+$  pair. This is consistent with the observed increase in the degradation rate of methylene blue for these samples. FESEM images confirm the increase in agglomeration size, accompanied by the presence of some small voids for annealed samples and also for samples made with higher temperature sol. This provides additional effective surface area and correspondingly more active sites available to enhance the degradation pathway and thus increase the degradation rate. This enhancement was also consistent



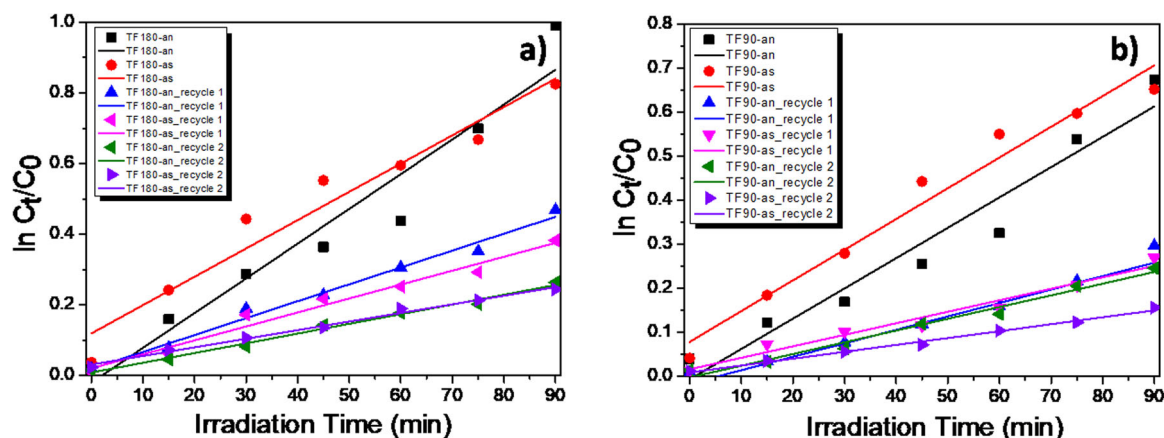
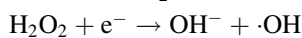
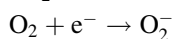
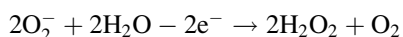


**Fig. 15** Determination of rate constant of dye degradation using photocatalyst made from (a) 90 °C sol, after first use and two recycles and (b) 180 °C sol, after first use and two recycles

with the relative peak intensities obtained from PL studies.  $I_{uv}/I_{blue}$  values decreased with annealing and higher hydrothermal temperature indicating higher number of defect sites. These defect states work as the trap centre for the photo-generated electron-hole pairs, restricting  $e^-/h^+$  recombination. When oxygen vacant states are annihilated by capturing ambient oxygen,  $O_2^-$  super ion species are created which reduces the recombination of photo-generated electrons and holes and generates hydroxyl radicals and peroxide ions [45].



These radicals and peroxide ions play a prominent role in oxidizing organic materials enhancing the photo-degradation rates. In the PL emission spectra green emission is mostly related to oxygen vacancies. Thus, lower values of  $I_{uv}/I_{green}$  in the PL emission spectra indicate the generation of more oxygen vacancies, thus promoting the photocatalytic activity for annealed and higher temperature samples.

To examine the stability of the photocatalyst we have repeated the photo-degradation process with each of the prepared sample twice more and observed that when we use them for the second time (recycle 1) degradation rate drops significantly. After a third use, it decreases to around 20% degradation of the dye after 90 min irradiation, as illustrated in Fig. 16.

The photo-degradation efficiencies of the reported thin films are below many of the values reported to date in the literature. However, most of the superior photo-efficiencies reported so far are for bulk  $TiO_2$ . For titania thin films, achieving a high rate of photo-degradation requires considerably longer reaction times, with several reports being

available in which reaction times of up to 100 h were used. The area of the photocatalyst thin film is also important. The films used in this study had a very small area of 1.5 cm × 1 cm, which limited the contact area of the  $TiO_2$  particles with the dye solution. Increasing the available area of the thin film would be expected to produce better results. Since the particles are in agglomerated form, it could reduce the porosity of the catalyst. Thereby access of the dye molecules could be prevented into inter-particle porous surface and reduce the surface area available for the dye adsorption. A possible solution is to use stearic acid as capping agent in the sol-gel method to prevent the agglomeration of small size nanoparticles due to surface repulsion. When the first run of the photo-degradation was completed, residual dye molecules were adsorbed on the surface of the photocatalyst. This resulted in a decrease in the available catalyst surface for generating hydroxyl radicals which reduced the photocatalytic activity of the catalysts when they were used repeatedly. In addition, the presence of oxygen vacancies, which was confirmed from the PL spectroscopy, act as electron trap sites for charge separation. However, after several cycles, the oxygen vacancies captured fewer electrons, leading to a high rate of electron-hole recombination. Hence the photocatalytic efficiency is reduced after several photocatalysis reactions. The reduction in the efficiency can also be attributed to the loss of photocatalyst film between the cycle runs and some refractory intermediates adsorbed on the surface which are difficult to decompose.

## 4 Conclusions

Anatase titania thin films were prepared by hydrothermal assisted sol-gel dip coating. The hydrothermal process to obtain the sols was carried out at two different temperatures, viz. 90 °C and 180 °C for 12 h each. For each hydrothermal

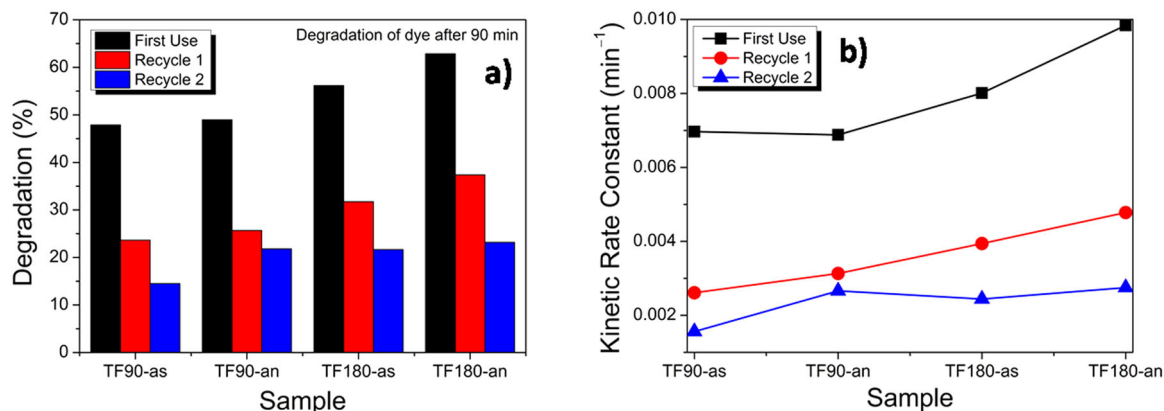


**Fig. 16** **a** Degradation of dye after 90 min of UV irradiation and **b** corresponding rate constant of all the samples after first use and two recycles

temperature, selected samples were annealed at 500 °C for 6 h. Anatase TiO<sub>2</sub> was obtained without the presence of any amorphous background at a temperature as low as 90 °C, even without any post deposition thermal treatment. This is a highly desirable property of TiO<sub>2</sub> thin films, but very rarely reported to date. Increasing hydrothermal temperature or imposing annealing treatment did not bring about any phase change and ended up only in crystallinity improvement with larger crystallite sizes indicating good thermal stability of the prepared anatase titania films. Besides crystallite sizes, increasing hydrothermal temperature and annealing had a significant impact on the nanostructural morphology of the films, including both the shapes and sizes of crystallites and agglomerates which directly influenced the surface properties and optical behavior of the thin films. Both RMS and average surface roughness increased with increased hydrothermal temperature and annealing, consistent with the observed increase in agglomerate size. The thin films maintained a Gaussian particle size distribution even after increasing hydrothermal temperature and annealing, emphasizing the good thermal stability of the films in terms of their phase and surface states. The porous structures with small spherical particles provide sufficient surface sites and pathway for a liquid to penetrate. These can be useful features for their potential use as photoanodes in dye sensitized solar cells. The indirect optical band gap of the films has been estimated to be in the range 3.08–3.22 eV by UV-VIS-NIR spectrophotometry, due to which these films can serve as a photoanode layer for photovoltaic devices. The inter-band region of the synthesized nanoparticles was composed of different levels of defect bands mostly related to self-trap excitons, surface state emissions and oxygen vacancies. Some of these trap states were annihilated by thermal treatment due to improvement in crystal structure and a reduction in the number of oxygen-vacancy-related defects. Thus, relative PL peak intensities falling in the green region

decreased significantly, whereas this decrease in the case of violet and blue emission was much less due to the thermal stability of the nanostructures. Since photocatalysis in metal oxides is mostly related to green emission, i.e. on oxygen vacancy states, this phenomenon improved the photocatalytic activity of the prepared films as a result of annealing and increased synthesis temperature. A reduction in the number of oxygen vacancies that can act as centers for e<sup>-</sup>/h<sup>+</sup> recombination promoted effective charge separation, contributing to better photocatalytic performance. The degradation of methylene blue dye after 90 minutes of photo-reaction by the as-deposited photocatalysts improved from 48% to 56% when the hydrothermal temperature was raised. A similar improvement from 49% to 63% was also observed for annealed samples. This degradation efficiency was obtained with a very small area (1.5 cm × 1 cm) of photocatalyst within only 90 minutes.

**Acknowledgements** Authors thank the ACMS, IIT Kanpur for providing XRD facility. Authors are grateful to Central Research Facility (CRF), IIT (ISM) Dhanbad for providing UV-Vis NIR spectroscopy, FESEM and AFM facility. We also acknowledge DST-FIST facility (project no. SR/FST/PSI-004/2013) for providing the photoluminescence spectrometer facility.

## Compliance with ethical standards

**Conflict of interest** We confirm that there are no known conflicts of interest associated with this publication and there has been no significant financial support for this work that could have influenced its outcome. The data that support the findings of this study are available from the corresponding author upon reasonable request. We confirm that the manuscript has been read and approved by all named authors and that there are no other persons who satisfied the criteria for authorship but are not listed. We further confirm that the order of authors listed in the manuscript has been approved by all of us.

**Publisher's note** Springer Nature remains neutral with regard to jurisdictional claims in published maps and institutional affiliations.

## References

- Bennett JM, Pelletier E, Albrand G, Borgogno JP, Lazarides B, Carniglia CK, Schmall RA, Allen TH, Tuttle-Hart T, Guenther KH, Saxer A (1989) Comparison of the properties of titanium dioxide films prepared by various techniques. *Appl Opt* 28 (16):3303–3317
- Chen JS, Chao S, Kao JS, Lai GR, Wang WH (1997) Substrate-dependent optical absorption characteristics of titanium dioxide thin films. *Appl Opt* 36(19):4403–4408
- Laube M, Rauch F, Ottermann C, Anderson O, Bange K (1996) Density of thin TiO<sub>2</sub> films. *Phys Res Sect B* 113(1-4):288–292
- Pulker HK, Paesold G, Ritter E (1976) Refractive indices of TiO<sub>2</sub> films produced by reactive evaporation of various titanium–oxygen phases. *Appl Opt* 15(12):2986–2991
- Tipparach U, Wongwanwatthana P, Sompan T, Saipin T, Krongkitsiri P (2008) Preparation and characterization of nano-TiO<sub>2</sub> thin films by sol-gel dip-coating method. *Nanotechnology* 7:129–136
- Tahar T, Mohamed A, Ilhem H, Azeddine C, Boubekeur B, Alexis F, Azzeddine B, Abdellaziz D (2014) Effects of dip-coating speed and annealing temperature on structural, morphological and optical properties of sol-gel nanostructured TiO<sub>2</sub> thin films. *Eur Phys J Appl Phys* 67(3):30302
- Pedrini LFK, Escalante LC, Scalvi LVA (2021) Deposition of TiO<sub>2</sub> thin Films by Dip-Coating Technique from a Two-Phase Solution Method and Application to Photocatalysis. *Materials Research* 24.
- Hengbo Y, Yuji W, Takayuki K, Shingo K, Sadao M, Hirotarō M, Takao S, Shozo Y (2001) Hydrothermal synthesis of nanosized anatase and rutile TiO<sub>2</sub> using amorphous phase TiO<sub>2</sub>. *J Mater Chem* 11:1694–1703
- Song S, Jing L, Li S, Fu H, Luan Y (2008) Superhydrophilic anatase TiO<sub>2</sub> film with the micro- and nanometer-scale hierarchical surface structure. *Mater Lett* 62(20):3503–3505
- Jia-Guo Y, Huo-Gen Y, Bei C, Xiu-Jian Z, Jimmy CY, Wing-Kei H (2003) The Effect of Calcination Temperature on the Surface Microstructure and Photocatalytic Activity of TiO<sub>2</sub> Thin Films Prepared by Liquid Phase Deposition. *J Phys Chem B* 107 (50):13871–13879
- Angulo-Ibáñez A, Goitandia AM, Albo J, Aranzabe E, Beobide G, Castillo O, Pérez-Yáñez S (2021) Porous TiO<sub>2</sub> thin film-based photocatalytic windows for an enhanced operation of optofluidic microreactors in CO<sub>2</sub> conversion. *Iscience* 24(6):102654.
- Naoki S, Hiroshi S (2021) Influence of vacuum environment on photocatalytic degradation of methyl red by TiO<sub>2</sub> thin film. *Acta Astronautica* 178:693–699
- Jinyu Z, Hua Y, Xinjun L, Shanqing Z (2008) Enhanced photocatalytic activity of TiO<sub>2</sub> nano-structured thin film with a silver hierarchical configuration. *Appl Surf Sci* 254(6):1630–1635
- Baba K, Simon B, Patrick C, Boscher ND (2017) Photocatalytic anatase TiO<sub>2</sub> thin films on polymer optical fiber using atmospheric-pressure plasma. *ACS Appl Mater Interfaces* 9(15):13733–13741
- Sreethawong T, Ngamsinlapasathian S, Yoshikawa S (2014) Positive role of incorporating P-25 TiO<sub>2</sub> to mesoporous-assembled TiO<sub>2</sub> thin films for improving photocatalytic dye degradation efficiency. *J Colloid Interface Sci* 430:184–192. <https://doi.org/10.1016/j.jcis.2014.05.032>
- Rahman KH, Kar AK (2021) Oxygen Vacancy and Adsorbed Superoxides Dependent Photocatalytic Activity of TiO<sub>2</sub> Quantum Dot Thin Films for Degradation of Methylene Blue with Variation of Precursor Concentration. *ECS J Solid State Sci Technol* 10 (8):081011
- Ge L, Xu M, Fang H, Sun M (2006) Preparation of TiO<sub>2</sub> thin films from autoclaved sol containing needle-like anatase crystals. *Appl Surf Sci* 253(2):720–725
- Yuan J, Tsujikawa S (1995) Characterization of sol-gel-derived TiO<sub>2</sub> coatings and their photoeffects on copper substrates. *J Electrochem Soc* 142(10):3444
- Dutta S, Leeladhar, Pandey A, Thakur OP, Pal R (2015) Electrical properties of ultrathin titanium dioxide films on silicon. *J Vac Sci Technol A: Vac, Surf, Films* 33(2):021507. <https://doi.org/10.1116/1.4904978>
- Karuppasamy A, Subrahmanyam A (2007) Studies on the room temperature growth of nanoanatase phase TiO<sub>2</sub> thin films by pulsed DC magnetron with oxygen as sputter gas. *J Appl Phys* 101(6):064318
- Wang M, Wang J, Chen W, Cui Y, Wang L (2006) Effect of pre-heating and annealing temperatures on quality characteristics of ZnO thin film prepared by sol–gel method. *Mater Chem Phys* 97:219
- Liu YC, Tung SK, Hsieh JH (2006) Influence of annealing on optical properties and surface structure of ZnO thin films. *J Cryst growth* 287(1):105–111
- Lin Y, Xie J, Wang H, Li Y, Chavez C, Lee S, Foltyn SR, Crooker SA, Burrell AK, McCleskey TM, Jia QX (2005) Green luminescent zinc oxide films prepared by polymer-assisted deposition with rapid thermal process. *Thin Solid Films* 492(1-2):101–104
- Arthararieswaran VP, Kumaravel A, Saravanakumar SS (2015) Physico-chemical properties of alkali-treated Acacia leucophloea fibers. *Int J Polym Anal Charact* 20(8):704–713
- Rajesh Kumar B, Subba Rao T (2012) AFM studies on surface morphology, topography and texture of nanostructured zinc aluminum oxide thin films. *Dig J Nanomater Biostruct* 7(4):1881–1889
- Rough Surfaces; HC Ward, Rough Surfaces, (1982), Profile Characterization, Chapter 4 in: TR Thomas Ed., Longman, London
- Lekshmy SS, Daniel GP, Joy K (2013) Microstructure and physical properties of sol gel derived SnO : Sb thin films for optoelectronic applications. *Appl Surf Sci* 274:95–100
- Shei S.-C., (2013) Optical and Structural Properties of Titanium Dioxide Films from TiO<sub>2</sub> and Ti<sub>3</sub>O<sub>5</sub> Starting Materials Annealed at Various Temperatures. *Adv Mater Sci Eng*, 2013: 1–7; 545076; <https://doi.org/10.1155/2013/545076>
- Zhang F, Zheng Z, Ding X, Mao Y, Chen Y, Zhou Z, Yang S, Liu X (1997) Highly oriented rutile-type TiO<sub>2</sub> films synthesized by ion beam enhanced deposition. *J Vac Sci Technol A: Vac, Surf, Films* 15(4):1824–1827
- Fujii T, Sakata N, Takada J, Miura Y, Daitoh Y, Takano M (1994) Characteristics of titanium oxide films deposited by an activated reactive evaporation method. *J Mater Res* 9(6):1468–1473
- Pandiaraman M, Soundararajan N, Vijayan C (2011) Effect of thickness on the optical band gap of silver telluride thin films. *J Ovonic Res* 7(1):21–27
- Humayan Kabir M, Mintu Ali M, Abdul Kaiyum M, Rahman MS (2019) Effect of annealing temperature on structural morphological and optical properties of spray pyrolyzed Al-doped ZnO thin films. *J Phys Commun* 3:105007
- Bashar MS, Matin R, Sultana M, Siddika A, Rahaman M, Gafur MA, Ahmed F (2020) Effect of rapid thermal annealing on structural and optical properties of ZnS thin films fabricated by RF magnetron sputtering technique. *J Theor Appl Phys* 14(1):53–63
- Kabir MH, Ali MM, Kaiyum MA, Rahman MS (2019) Effect of annealing temperature on structural morphological and optical properties of spray pyrolyzed Al-doped ZnO thin films. *J Phys Commun* 3(10):105007
- Tan T-T, Liu B-J, Wu Z-H, Liu Z-T (2017) Annealing Effects on Structural, Optical Properties and Laser-Induced Damage Threshold of MgF<sub>2</sub> Thin Films. *Acta Metall Sin (Engl Lett)* 30 (1):73–78. <https://doi.org/10.1007/s40195-016-0479-x>
- Sahoo D, Priyadarshini P, Aparimita A, Alagarasan D, Ganesan R, Varadarajaperumal S, Naik R (2020) Role of annealing temperature on optimizing the linear and nonlinear optical properties

- of  $\text{As}_{40}\text{Se}_{50}\text{Ge}_{10}$  films. *RSC Adv* 10:26675–26685. <https://doi.org/10.1039/D0RA04763E>
37. Loubna C, Tetiana B, Nikolay Polikarpovich K, Djamel H, Sahraoui C, Slimane A (2017) Photoluminescence properties of  $\text{TiO}_2$  nanofibers. *J Nanopart Res* 19:129. <https://doi.org/10.1007/s11051-017-3822-x>
  38. Liu B, Zhao X, Wen L (2006) The structural and photoluminescence studies related to the surface of the  $\text{TiO}_2$  sol prepared by wet chemical method. *Mater Sci Eng: B* 134(1):27–31
  39. Santara B, Giri PK, Imakita K, Fujii M (2013) Evidence of oxygen vacancy induced room temperature ferromagnetism in solvothermally synthesized undoped  $\text{TiO}_2$  nanoribbons. *Nanoscale* 5(12):5476–5488
  40. Lei Y, Zhang LD, Meng GW, Li GH, Zhang XY, Liang CH, Chen W, Wang SX (2001) Preparation and photoluminescence of highly ordered  $\text{TiO}_2$  nanowire arrays. *Appl Phys Lett* 78:1125
  41. Zuo F, Wang L, Wu T, Zhang Z, Borchardt D, Feng P (2010) Self-doped  $\text{Ti}^{3+}$  enhanced photocatalyst for hydrogen production under visible light. *J Am Chem Soc* 132:11856
  42. Justicia I, Ordejon P, Canto G, Mozos JL, Fraxedes J, Battiston GA, Gerbasi R, Figueras A (2002) Designed self-doped titanium oxide thin films for efficient visible-light photocatalysis. *Adv Mater* 14:1399
  43. Li FB, Li XZ (2002) Photocatalytic properties of gold/gold ion-modified titanium dioxide for wastewater treatment. *Appl Catal A: Gen* 228(1-2):15–27
  44. Toyoda T, Hayakawa T, Abe K, Shigenari T, Shen Q (2000) Photoacoustic and photoluminescence characterization of highly porous, polycrystalline  $\text{TiO}_2$  electrodes made by chemical synthesis. *J Lumin* 87:1237–1239
  45. Li XQ, Qiao GJ, Chen J (2006) Photodegradation Mechanism of Oxygen Vacancies in Titanium Dioxide Modified by Radio Frequency Plasma. *J Chin. Ceram Soc* 34(12):1466–1469